

# High-precision efficiency calibration of a high-purity co-axial germanium detector

B. Blank<sup>a 1</sup> J. Souin<sup>a</sup> P. Ascher<sup>a</sup> L. Audirac<sup>a</sup> G. Cachel<sup>a</sup> M. Gerbaux<sup>a</sup> S. Grévy<sup>a</sup> J. Giovinazzo<sup>a</sup>  
 H. Guérin<sup>a</sup> T. Kurtukian Nieto<sup>a</sup> I. Matea<sup>a 2</sup> H. Bouzomita<sup>b</sup> P. Delahaye<sup>b</sup> G.F. Grinyer<sup>b</sup>  
 J.C. Thomas<sup>b</sup>

<sup>a</sup>Centre d'Etudes Nucléaires de Bordeaux Gradignan - UMR 5797, CNRS/IN2P3 - Université de Bordeaux, Chemin du Solarium, BP 120, 33175 Gradignan Cedex, France

<sup>b</sup>Grand Accélérateur National d'Ions Lourds, CEA/DSM - CNRS/IN2P3, Bvd Henri Becquerel, BP 55027, F-14076 CAEN Cedex 5, France

---

## Abstract

A high-purity co-axial germanium detector has been calibrated in efficiency to a precision of about 0.15% over a wide energy range. High-precision scans of the detector crystal and  $\gamma$ -ray source measurements have been compared to Monte-Carlo simulations to adjust the dimensions of a detector model. For this purpose, standard calibration sources and short-lived online sources have been used. The resulting efficiency calibration reaches the precision needed e.g. for branching ratio measurements of super-allowed  $\beta$  decays for tests of the weak-interaction standard model.

*Key words:* gamma-ray spectroscopy, super-allowed beta transitions, germanium detector, Monte-Carlo simulations

*PACS:* 07.85.-m, 29.30.Kv, 23.20.-g

---

## 1. Introduction

Many spectroscopic studies in nuclear physics require only modest precisions (typically of the order of 1-10%) simply because nuclear-structure or astrophysical models are limited in their precision and therefore in their predictive power due to the lack of a high-precision standard model in nuclear physics. However, studies at the interface between nuclear and particle physics, where the nuclear  $\beta$  decay is used as a probe, require precisions which go well beyond the above mentioned level. Nuclear  $0^+ \rightarrow 0^+$   $\beta$  decay is presently the most precise means to determine the weak-interaction vector coupling constant  $g_V$  which, together with the coupling constant for muon decay, allows the determination of the  $V_{ud}$  matrix element of the Cabibbo-Kobayashi-Maskawa (CKM) quark mixing matrix. To determine this matrix element, the  $\beta$ -decay Q value, the half-life and the super-allowed  $0^+ \rightarrow 0^+$  branching ratio have to be measured with a relative precision of about 0.1%. Q-value determination has become "quite easy" with the use

of Penning-trap mass spectrometry where precisions well below 1 keV, equivalent to some  $10^{-4}$  relative precision, are now routinely reached for most of the nuclei of interest. The half-life is usually determined by  $\beta$ -particle or  $\gamma$ -ray counting and precisions of the half-lives well below  $10^{-3}$  are obtained [1].

In these measurements, the precise determination of the branching ratio remains the tricky part, in particular in more exotic nuclei (e.g. nuclei with an isospin projection  $T_z = -1$ ) where the non-analogue branches, i.e. the branches other than the  $0^+ \rightarrow 0^+$   $\beta$ -decay branch, are of the same order of magnitude as the analogue branch. As, due to a continuous spectrum, it is extremely difficult to determine these branching ratios by a measurement of the  $\beta$  particles, the branching ratios are usually determined by detecting  $\gamma$  rays de-exciting the levels populated by  $\beta$  decay by means of germanium detectors. Therefore, in order to determine a branching ratio with a precision of the order of 0.1%, one needs to know the absolute efficiency of a germanium detector with a similar or better precision.

To our knowledge, there is presently one germanium detector which is efficiency calibrated to such a precision [2–4]. The calibration of a single-crystal high-purity co-axial germanium detector we present here will therefore follow to

<sup>1</sup> Corresponding author: B. Blank, blank@cenbg.in2p3.fr

<sup>2</sup> Permanent address: Institut de Physique Nucléaire, 15 rue Georges Clémenceau, 91406 Orsay Cedex, France

some extent the procedure used by Hardy and co-workers.

The aim of the present work is to construct a detector model using a simulation tool able to calculate detection efficiencies in different environments for any radioactive source or  $\gamma$ -ray energy. For this purpose, we have used a 3D detector scan and 23 different radioactive sources to calibrate our detector in full-energy peak as well as in total efficiency and we have tuned our detector model to match the source measurements. As will be laid out in detail below, we used 10 sources to determine the total-to-peak (T/P) ratio, and 14 sources for the peak efficiency determination, a dedicated  $^{60}\text{Co}$  source being used in both series of measurements. For the simulations, we used mostly the CYLTRAN code [5] which was upgraded to allow for the simulation of complete decay schemes of radioactive sources. We also added the process of positron annihilation-in-flight originally not present in the code. In a later stage of our work, we implemented our detector model also in GEANT4 [6] and found perfect agreement between the two codes, with the CYLTRAN code being much faster than GEANT4 and GEANT4 allowing for more flexibility of the geometry of the problem simulated.

## 2. Detector, electronics, and data acquisition

The detector we purchased for the present work is an n-type high-purity co-axial germanium detector with a relative efficiency of about 70%. An n-type detector is important in particular for detecting low-energy  $\gamma$  rays, as the thick dead zone for an n-type detector is on the inner surfaces of the detector and, in particular, not on the front surface facing the radioactive sources. We have chosen an aluminum entrance window instead of a much more fragile beryllium window, because the detector will travel to different laboratories. A large dewar ensures an autonomy of the detector of close to four days.

A X-ray photography of the detector (Fig. 1) shows a slight tilt of approximately  $1^\circ$  of the detector crystal in the aluminum can. GEANT4 simulations lead us to the conclusion that this tilt has no influence on the results of the present work. The initial manufacturer characteristics of the detector, used as a starting point for the simulations, are given in Tab. 1.

As in the work of Hardy and co-workers, we used a fixed source - detector distance of 15 cm. This distance allows us to reach a positioning precision of  $10^{-3}$  even in more difficult online conditions with radioactive sources deposited on a tape transport system.

The experiment electronics consists mainly of an ORTEC 572A spectroscopy amplifier, an ORTEC 471 timing filter amplifier, and an ORTEC 473A discriminator. The signal from the discriminator is then sent to a LeCroy 222 gate generator (gate length typically a few micro-seconds) which then triggers the data acquisition (DAQ). The measurement duration is determined with a high-precision pulse generator (relative precision of  $10^{-5}$ ) fed into a CAEN

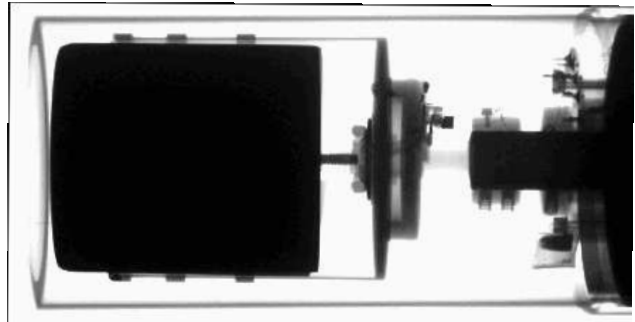


Fig. 1. X-ray photograph of the germanium detector. The slight tilt of the crystal with respect to the detector housing (about 1 degree) is visible.

VME scaler (V830) in the DAQ.

The data acquisition is a standard GANIL data acquisition [7] using VME modules. In addition to the scaler, we use a V785 ADC from CAEN for the energy signals and the TGV trigger unit built by LPC Caen [8].

Table 1

Detector characteristics used in the modelling of the germanium detector. The vendor specifications are compared to the finally adopted characteristics.

	vendor specifications	adjusted parameters
length of crystal	79.2 mm	78.10 mm
radius of crystal	34.8 mm	34.66 mm
length of central hole	59.5 mm <sup>1</sup>	71.59 mm
radius of central hole	5.0 mm	7.8 mm
external dead zone	< 0.5 $\mu\text{m}$	0.5 $\mu\text{m}$
internal dead zone	0.5 mm	0.5 mm
back-side dead zone	0.5 mm	1 mm
distance window - crystal	5 mm	5.73 mm
entrance window thickness	7 mm	7 mm

The dead-time correction is performed by means of a 1 kHz pulser sent directly to the scaler and passed through a veto module (Phillips 758), where the veto is generated by the BUSY signal of the DAQ. The live-time (LT) is the ratio between the second and the first scaler values and the dead-time (DT) is equal to  $1 - \text{LT}$ . To test the dead-time correction, a radioactive source ( $^{137}\text{Cs}$ ) was mounted on the source holder at 15 cm from the detector entrance window. A measurement yielded a first result for the counting rate in the detector. We then added other triggers from a pulse generator. Thus the trigger rate of the DAQ was steadily increased without affecting the number of  $\gamma$  rays emitted from the  $^{137}\text{Cs}$  source hitting the detector. Without dead-time correction, the apparent counting rate from the source decreases with increasing total trigger rate. When corrected for the acquisition dead time as described above, we recover

<sup>1</sup> A value given later by the vendor was 70.0(5) mm.

the source counting rate without dead-time. We performed similar tests also with a  $^{60}\text{Co}$  source (twice higher  $\gamma$ -ray energies) and found equivalent results.

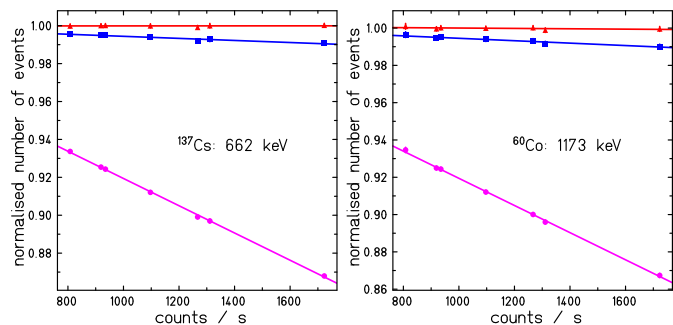


Fig. 2. Dead-time and pile-up corrections as described in the text. The constant counting rate of a  $^{137}\text{Cs}$  source (left-hand side) is recovered after correcting for the acquisition dead-time and the signal pile-up. Similar results are obtained for the  $^{60}\text{Co}$  source (right-hand side). The purple curves (full circles) correspond to the uncorrected data, the blue lines (full squares) to the data corrected only for the dead-time, and the red lines (full triangles) represent the data corrected for both, the dead-time and the pile-up.

Another concern when aiming for very high detection efficiency precision is the pile-up of radiation in the detector. Due to summing of signals from different events, counts are removed from the full-energy peak of a  $\gamma$  ray and moved to higher energy. We correct this by assuming a Poisson distribution of the events around a measured average count rate. With this assumption, we can determine the pile-up probability once we have defined a "pile-up time window" [9]. This time window was determined in a similar fashion as the dead-time correction. The full-energy peak counting rate was determined for a fixed source ( $^{137}\text{Cs}$  or  $^{60}\text{Co}$ ). In a second step, a low-energy source ( $^{57}\text{Co}$ ) was approached more and more to increase the trigger rate, but also the pile-up. In the analysis, the pile-up time window was varied to achieve a full-energy peak rate of the fixed source independent from the total counting rate of the detector. The results of this procedure are shown in Fig. 2. It was found experimentally that the pile-up time window depends, as expected, linearly on the shaping time of the amplifier ( $2.75 \times$  shaping time) and is, at least in the limit of the precision we achieved, independent of the  $\gamma$ -ray energy. This last finding is not necessarily expected, as, e.g. in a too large acquisition window, a larger signal coming after a smaller one will "erase" this smaller signal in our peak-sensing ADC.

All measurements except those for the dead-time and pile-up correction measurements, in particular those for the determination of the absolute efficiency with the  $^{60}\text{Co}$  source, were performed with counting rates well below 1000 counts per second where the dead-time and the pile-up are relatively small and can be therefore reasonably well corrected for.

### 3. Monte-Carlo simulations

As explained above, the aim of this work is to construct a model for a simulation code which allows us to determine the detection efficiency of the germanium detector in different environments, for any source and  $\gamma$ -ray energy. Several codes have been used for similar purposes. We have chosen the CYLTRAN [5] and the GEANT4 [6] Monte-Carlo (MC) codes. The large majority of the simulations were performed with the CYLTRAN code, mainly because this code was largely tested for  $\gamma$ -ray and electron transport (e.g. in [2–4]) and because it is about a factor of four faster than the GEANT4 code. However, the CYLTRAN code has the draw-back that the geometry has to be cylindrical which limits the flexibility of the simulations to some extent. In addition, the original version of the code did not allow for the simulation of complete decay schemes. In fact, only a single-energy  $\gamma$  ray or electron was admitted as the input particle or an electron spectrum defined by the user. Finally, as mentioned above, positron annihilation in-flight was not taken into account in the code. However, it should be underlined also that the decay schemes implemented in GEANT4 are not usable for our purpose, because first of all some of them are faulty and none of them include angular correlation in  $\gamma - \gamma$  cascades. In the simulations, we performed, the same external event generator was used for both MC codes.

#### 3.1. CYLTRAN upgrade and event generation

##### 3.1.1. Annihilation in-flight

As mentioned above and found in ref. [4], annihilation-in-flight (AIF) of positrons was not included in the Monte-Carlo code CYLTRAN. Therefore, in the work of Helmer et al. [4], the escape probabilities had to be corrected for with a procedure described in the Table of Isotopes [10]. We corrected the CYLTRAN code and included AIF in a way consistent with all other interactions. The cross-section calculations were taken from the GEANT3 code [11] and the probability of annihilation in-flight was added to the other interaction probabilities in the code where appropriate. The correct functioning of this new part of the code was tested with the comparison of the single- and double-escape probabilities for high-energy  $\gamma$  rays interacting in the detector.

In a first step, we compared in a calculation the number of counts in the full-energy peak as well as the single- and double-escape peaks to measurements and found excellent agreement. A more quantitative agreement can be seen in Fig. 3. The ratios of single-escape over full-energy peaks as well as of double-escape over full-energy peaks from our source measurements are compared to simulations with the modified CYLTRAN code. Although for some of the ratios some disagreement exists, mainly due to difficulties to fit relatively small peaks, a very satisfactory overall agreement is found and demonstrates that the AIF probabilities are now correctly taken into account in the program.

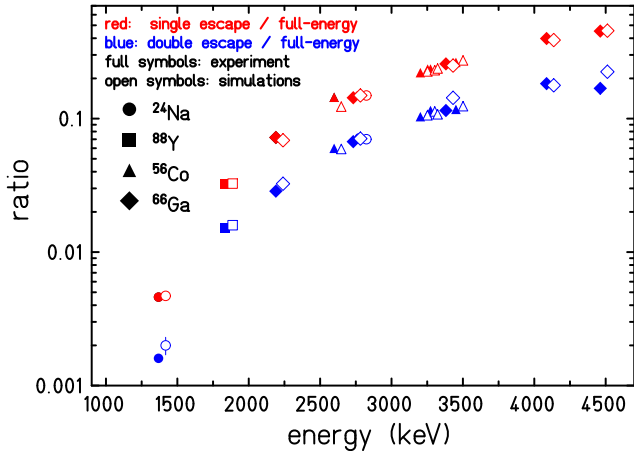


Fig. 3. Ratios of single-escape over full-energy intensity (red) as well as of double-escape over full-energy intensity (blue) from source measurements with  $^{24}\text{Na}$ ,  $^{88}\text{Y}$ ,  $^{56}\text{Co}$ , and  $^{66}\text{Ga}$ . Full symbols represent experimental ratios, open symbols are from simulations with the CYLTRAN code (simulation results are slightly shifted with respect to experimental data for a better lisibility). Very good agreement is obtained from the lowest to the highest energies.

### 3.1.2. Simulation of full decay events

In order to allow for the simulation of complete decay schemes including  $\beta$  decay, electron capture,  $\gamma$ -ray cascades, conversion electrons, Auger electrons, and X-rays, the code was upgraded to allow for several particles or  $\gamma$  rays as input for one event. In fact, several particles in a single event were already treated in the code, as long as they were produced as secondary particles during the event (e.g. by electron-positron pair production, by Compton scattering where an electron and a  $\gamma$  ray are created). However, only one particle was allowed at the beginning of an event. This upgrade was done similar to the treatment of secondary particles, i.e. they were added in a stack of particles for an event which are then treated one by one.

The generation of a decay event is done in a separate program which generates these complete events and writes them into a file which is then read in by either CYLTRAN or GEANT4 for the simulation of a germanium spectrum of e.g. a  $^{60}\text{Co}$  source. The input data needed to generate the decay events were principally (see Tab. 2) taken from the Evaluated Nuclear Structure Data Files (ENSDF) from the National Nuclear Data Center in Brookhaven [12], from the Atomic Mass Evaluation [13], and from the Table of Isotopes [10], appendices F-3 and F-4. With these inputs we were able to achieve the  $\gamma$  and X-ray branching ratios given in the latest IAEA evaluations [14,15]

Evidently, once the input event set is correctly generated, the simulation deals correctly with effects like coincident summing, the effect of angular correlations in  $\gamma - \gamma$  cascades etc. Therefore, the yields obtained for the full-energy peaks observed in the simulations are directly comparable to the results from the measurements with radioactive sources, once effects of dead-time and pile-up are corrected for or negligible. However, this procedure has also some

draw-backs. For example, the emission angle of  $\gamma$  rays in the simulations can no longer be limited to the opening cone of the germanium detector, but a  $4\pi$  simulation has to be performed in all cases which leads to very long simulation times. In a similar way, the environment around the detector in addition to the detector housing has to be present in the simulations, because the total-to-peak ratio has to be correct from the beginning and can not be corrected by a factor as done e.g. in [2–4]. However, we have now the possibility to calculate efficiencies for single-energy  $\gamma$  rays as well as for spectra from any source, as long as the necessary input data are available.

### 3.2. Detector model

The detector model used in the simulations is shown in Fig. 4. The version shown is the one used in the CYLTRAN simulations. However, the only differences between the CYLTRAN and GEANT4 models come from the fact the CYLTRAN knows only cylinders. Therefore, the round

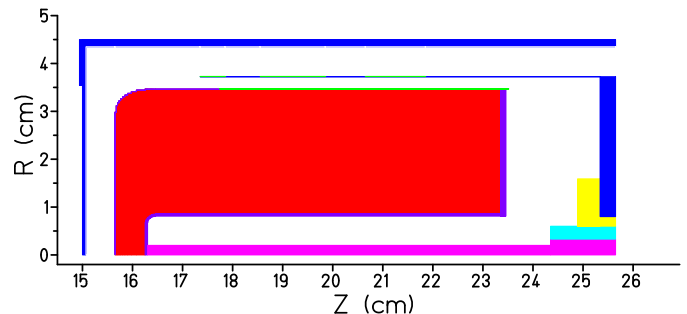


Fig. 4. Detector model as used in CYLTRAN simulations. The colour code is as follows: red: germanium; violet: germanium dead material; blue: aluminum; pink: brass. The green material corresponds to screws from the detector holding structure, which, in CYLTRAN, had to be "distributed" over a hollow cylinder. The other colours correspond to isolating material and teflon.

edges of the germanium crystal had to be constructed by adding many tiny cylinders to achieve an apparent round edge by keeping the germanium volume constant. In GEANT4, the use of a torus greatly simplifies the modelling task. The dimensions used in the final detector model are compared to the manufacturer data in Tab. 1. It is interesting to note that the central hole of the crystal is much longer and wider than given originally by the vendor.

Fig. 5 compares the simulation results from CYLTRAN and GEANT4 to experimental spectra. Although some deficiencies can be observed, e.g. a lack of counts below the full-energy peak and an overestimation of the number of counts and a different shape around the edge from  $180^\circ$  backscattering of Compton scattering events around 200–300 keV, the overall shape agreement is quite satisfying.

In these simulations, we used a detector resolution as determined experimentally. However, in the simulations which we discuss in the following and which were used to

Table 2

Source characteristics used to determine the detector efficiency. We give the error bar for the half-life of  $^{60}\text{Co}$ , as we use the absolute activity of this source.

Nuclide	$T_{1/2}$	$E_\gamma$ (keV)	$P_\gamma$ (%)	References	Nuclide	$T_{1/2}$	$E_\gamma$ (keV)	$P_\gamma$ (%)	References		
$^{24}\text{Na}$	14.9590 h	1368.6	99.9935(5)	[14]	$^{133}\text{Ba}$	11.551 y	30.6-30.9	96.8(11)	[15,14]		
		2754.0	99.872(8)				34.9-36.0	22.8(3)			
$^{27}\text{Mg}$	9.458 min	170.7	0.85(3)	[16]			53.2	2.14(3)			
		843.8	72.1(3)				79.6-81.0	35.55(35)			
		1014.4	27.9(3)				223.2	0.453(4)			
		$^{48}\text{Cr}$	21.56 h				112.3	98.34(4)		276.4	7.16(5)
308.2	99.473(5)			302.9			18.34(13)				
$^{56}\text{Co}$	77.236 d	846.8	99.9399(23)	[14]			356.0	62.05(19)			
		1037.8	14.03(5)				383.8	8.94(6)			
		1175.1	2.249(9)				$^{134}\text{Cs}$	753.5 d		475.4	1.49(2)
		1238.3	66.41(16)		563.2	8.37(3)					
		1360.2	4.280(13)		569.3	15.38(4)					
		1771.3	15.45(4)		604.7	97.65(2)					
		2015.2	3.017(14)		795.8	85.5(3)	$^{137}\text{Cs}$	30.09 y	31.8-32.2	55.4(8)	[14]
		2034.8	7.741(13)		801.9	8.70(3)					
		2598.8	16.96(4)		1038.6	0.990(5)					
		3201.9	3.203(13)		1168.0	1.792(7)					
		3253.6	7.87(3)		1365.2	3.017(12)					
		3273.0	1.855(9)		$^{152}\text{Eu}$	13.53 y			39.5-46.8	73.32(35)	
		3451.1	0.942(6)				121.8	28.41(13)			
		$^{60}\text{Co}$	1925.23(27) d		1173.2	99.85(3)	[14]	244.7	7.55(4)		
1332.5	99.9826(6)			344.3	26.58(12)						
$^{66}\text{Ga}$	9.304 h	833.5	5.906(19)	[17,18]	411.1	2.237(10)					
		1039.2	37.07(11)		444.0	3.125(14)					
		1333.1	1.177(4)		778.9	12.96(6)					
		2189.6	5.3457(19)		867.4	4.241(23)					
		2751.8	22.74(9)		964.1	14.62(6)					
		3228.8	1.513(7)		1085.8	10.13(6)					
		3380.9	1.468(7)		1089.7	1.731(10)					
		3422.0	0.858(5)		1112.1	13.40(6)					
		4085.9	1.277(7)		1212.9	1.415(9)					
		4806.0	1.865(11)		1299.1	1.632(9)					
$^{75}\text{Se}$	119.778 d	66.0	1.112(12)	[14]	1408.0	20.85(9)					
		97.0	3.42(3)		$^{180}\text{Hf}^m$	5.47 h	93.3	17.13(28)	[12]		
		121.0	17.2(3)				215.3	81.30(66)			
		136.0	58.2(7)				332.3	94.10(75)			
		199.0	1.48(4)				443.1	81.87(94)			
		265.0	58.9(3)		500.7	14.30(28)	$^{207}\text{Bi}$	32.31 y	72.8	21.69(24)	[14]
		279.0	24.99(13)		75.0	36.50(40)					
		303.0	13.16(8)		84.8	12.46(23)					
401.0	11.47(9)	87.6	3.76(10)								
$^{88}\text{Y}$	106.625 d	66.0	1.112(12)	[14]	569.7	97.76(3)					
		898.0	93.90(23)		1063.7	74.58(49)					
		1836.0	99.38(3)		1770.2	6.87(3)					

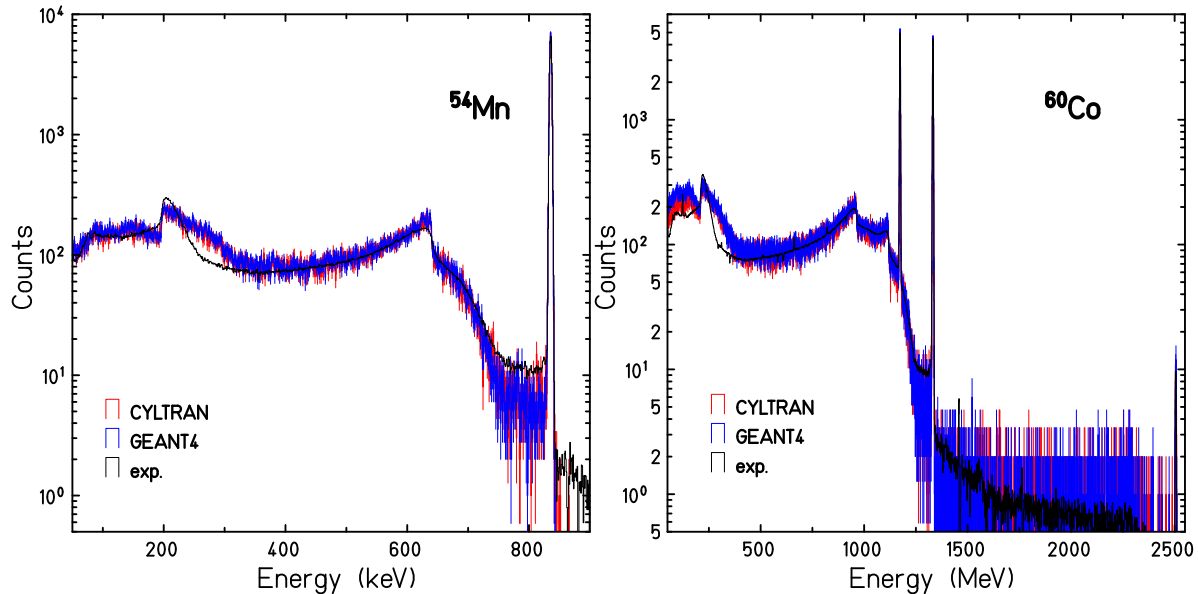


Fig. 5. Comparison of CYLTRAN and GEANT4 simulation with measurements using sources of  $^{54}\text{Mn}$  and  $^{60}\text{Co}$  with the final detector model including the environment around the detector. The different spectra are matched with the height of the full-energy peaks.

determine the peak and total efficiencies, we did not use a detector resolution in order to more easily determine the number of counts in a peak. The number of counts was determined from the number of counts in the channel of the full-energy peak from which the average number of counts of the five neighbouring channels left and right from the peak were subtracted as the background under the peak.

#### 4. Analysis of experimental data

##### 4.1. Analysis of detector scan data

The detector scans were performed at the AGATA detector scanning table at CSNSM [19] and at CENBG. At CSNSM, a strongly collimated  $^{137}\text{Cs}$  source with a  $\gamma$ -ray energy of 662 keV and an activity of about 477 MBq was used. Fig. 6 shows the detector installed on the X-Y scanning table at CSNSM. One- and two-dimensional scans were performed over the front of the detector as well as over the full length of the crystal. Typical step sizes were between 0.5 mm (one-dimensional scans) and 2 mm (two-dimensional scans). A measurement point lasted typically 20 s. The data were analysed by either integrating the full-energy peak or the total number of counts in the spectrum thus neglecting the small contribution from room background. As will be shown below, these scans allowed to fine tune the parameters of the detector model.

At CENBG, scans were performed with low-energy sources of  $^{57}\text{Co}$  and  $^{241}\text{Am}$ . In these scans, the sources were collimated only in one dimension, i.e. the sources viewed the detector through a one-millimeter slit. Steps of 1 mm and measurement times of 30 min were used. In this case, only the full-energy peak was integrated as a function of the position of the source.



Fig. 6. Photograph of the germanium detector installed on the scanning table at CSNSM. In the present position, the crystal side was scanned in two directions.

##### 4.2. Analysis of the radioactive source data

The experimental data for all source measurements were taken with a GANIL-type data acquisition [7]. The data



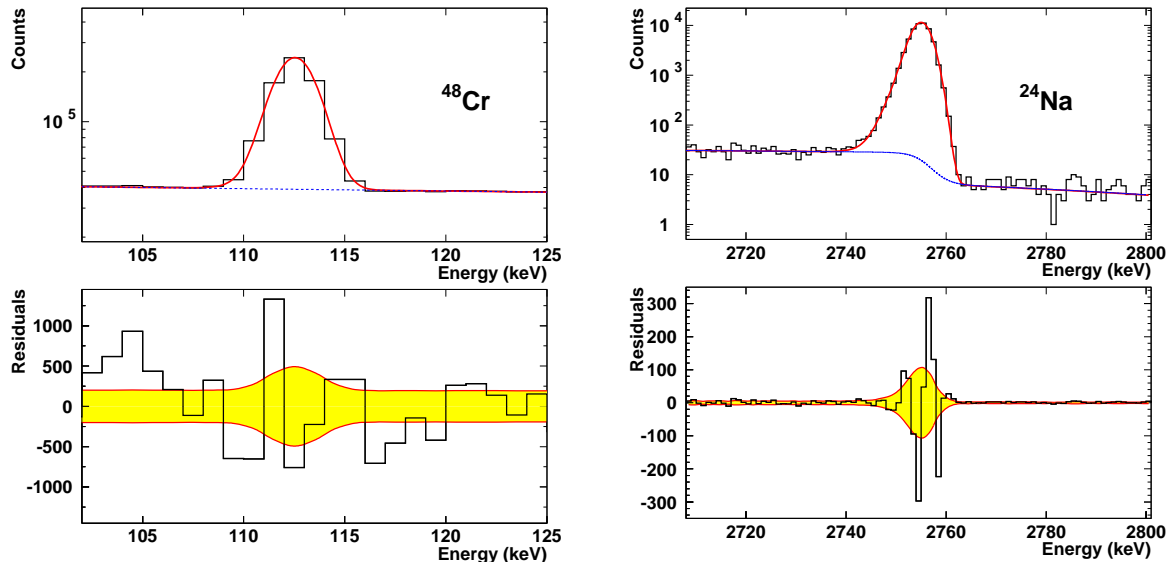


Fig. 7. Comparison of an experimental spectrum for a low-energy and a high-energy peak with the fit. The left-hand side shows a fit of the 112 keV peak of  $^{48}\text{Cr}$  and the right-hand side a fit of the 2754 keV line of  $^{24}\text{Na}$ . The histogram is the experimental spectrum, the red line is the fit, and the dashed blue line is the background function. The low-energy peak is fitted with a second-degree polynomial as the background, whereas a smoothed step function is used for the high-energy peak. The lower figures show the fit residuals. The black histograms are the residuals and the yellow bands are the statistical error bands.

were analysed using the PAW software [20]. In contrast to the work of Helmer *et al.* [3] who used only a simple Gaussian to fit the full-energy peaks, we fitted them with a function containing a Gaussian plus a low-energy tail described by a shifted asymmetric Gaussian to take into account the incomplete charge collection in the germanium crystal. To constrain the fit and reach a faster convergence, the tail parameters were first determined over a wide range of energies and then fixed in the fits as a function of the peak energy.

As the background function, we used three different descriptions: (i) a second-order polynomial, (ii) a linear step function (complement of an error function and a straight line), or (iii) two independent linear functions left and right of the peak "smoothly" connected under the peak. Out of these three functions, we chose for each peak the two most appropriate background functions to fit the peaks. For each peak, two fits were performed over a different fitting window yielding thus four different fits for each peak. The best fit in terms of the normalised  $\chi^2$  was kept with its error as determined from the fit. The second best fit was used to determine a systematic error from the difference of the two best fits which was added quadratically to the fit error from the best fit.

Fig. 7 shows the fit result for a low-energy and a high-energy peak together with the residuals from the experimental spectrum and the fit. Although it is evident that the function used to describe the full-energy peak is not complete, the integral of the peak is determined with high precision.

## 5. Experimental results and comparison with CYLTRAN simulations

In the following sections, we will first present the results from the detector scans which allowed for a fine adjustment of the detector model parameters. With this detector model, we will then compare the source measurements to simulations in order to verify that the detector model allows for an overall agreement between simulation and measurement over a wide range of  $\gamma$ -ray energies.

### 5.1. Results from detector scans

We have scanned the detector in three directions: (i) a scan on the front side of the detector, (ii) a scan parallel to the cylinder axis of the crystal, and (iii) a scan perpendicular to the cylinder axis. They are termed "front scan", "parallel scan", and "perpendicular scan", respectively, in the following.

Fig. 8 shows a comparison of the experimental scan results and the simulations. In particular, the scans with the  $^{137}\text{Cs}$  source allowed us to precisely adjust the detector model parameters. The figure shows that nice agreement is obtained for the full-energy peak for all scans, whereas some deficiencies remain for the total number of counts observed. This is due to the fact that for the full energy peak intensity, only the detector crystal itself is important, while for the total spectrum the environment around the detector influences the counting rate. As this environment is different from one experimental site to another, we did not insist too much in improving this aspect. The environment was

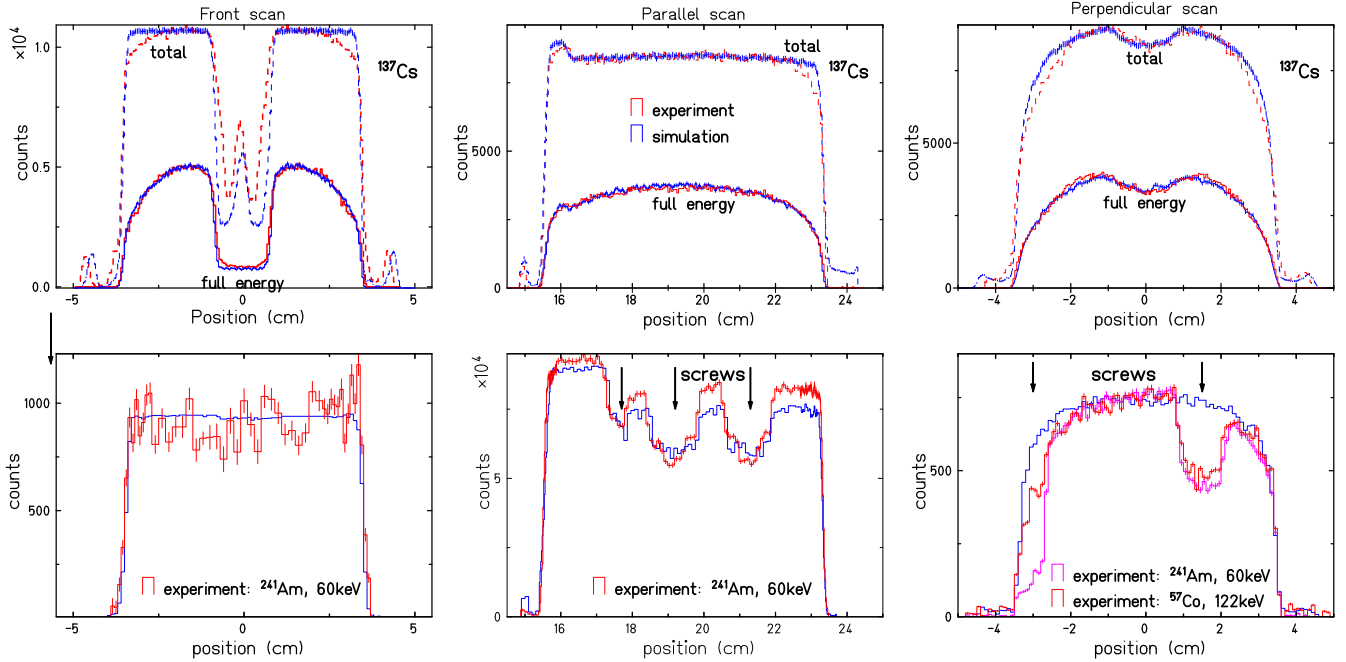


Fig. 8. Comparison of experimental data from the scans of the different detector dimensions with simulation performed with the CYLTRAN code. From left to right: Front scan, parallel scan, perpendicular scan. The  $^{137}\text{Cs}$  scans (top panels) yield a clear picture of the size of the crystal and its position in the detector can. In particular, the tilt of the crystal in the aluminum can can be seen by means of a shift of Compton scattering events from the detector can and the central rod between simulation and experiment, while the germanium crystal is perfectly aligned. In the total energy spectrum, the distance of the crystal from the entrance window could be determined in the parallel scan. The low-energy scans (lower panels) are affected by the holding structure of the crystal, mainly by the screws indicated in the figure, which absorbs to some extent these low-energy  $\gamma$  rays. This is seen with the scans with the  $^{57}\text{Co}$  source ( $E_\gamma = 122\text{keV}$ ) and the  $^{241}\text{Am}$  source ( $E_\gamma = 60\text{keV}$ ). In the perpendicular scan, the screws are not seen in the simulation, as they are "distributed" over a cylindrical ring.

adjusted in the simulations in order to reproduce the Total-to-Peak ratio (see below), the only important parameter related to the physical environment around the detector.

The scans with the low-energies sources performed at CENBG did not contribute as much to the detector parameter determination. This is mainly due to the fact that low-energy  $\gamma$  rays are, at least to some extent, absorbed in the material around the detector and notably by the crystal holding structure, as can be seen by the scans with the  $^{57}\text{Co}$  and  $^{241}\text{Am}$  sources. The screws used to fix the crystal within its housing absorb clearly a large part of the  $\gamma$  rays. Nonetheless, these measurements allowed us to verify the parameters determined with the high-energy scan.

On the parallel scan with the  $^{137}\text{Cs}$  source, one can see that the height of the total spectrum in the simulation is slightly larger than in the experimental data in the region of the entrance window. This might be an indication that the entrance window of the aluminum can is thinner than given by the manufacturer. Evidently this would influence the efficiency in particular for low-energy  $\gamma$  rays. In order to check this thickness, we performed measurements with a mono-energetic electron source.

## 5.2. Thickness of detector entrance window

At CENBG, the "Neutrino" group possesses a mono-energetic electron source made of a collimated electron beam from a strong  $^{90}\text{Sr}$  source which passes through a magnetic field to select a particular energy bin. After an energy calibration with low-energy  $\gamma$ -ray sources, we used electron energies of 0.8, 1.0, 1.4, and 1.8 MeV incident on the entrance window in a direction parallel to the detector axis. The electron peak position and thus the energy loss in the entrance window were compared to simulation with the CYLTRAN code for the same conditions.

In the simulations, we varied the thickness of the entrance window. As can be seen from Fig. 9, it is somewhat difficult to determine the exact peak position of the electrons, as the peak is much larger than a typical  $\gamma$ -ray peak. However, within a thickness range of 0.65 and 0.7 mm we found good agreement between experimental measurements and simulations. This thickness range includes the manufacturer's value of 0.7 mm. In the following, we will therefore use a thickness of 0.7 mm.



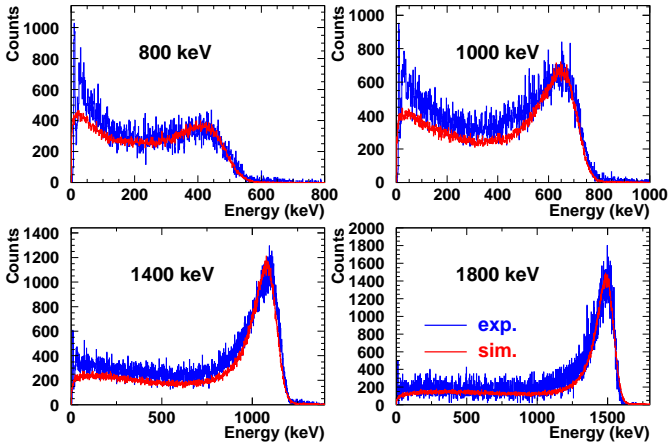


Fig. 9. Comparison of experimental data and simulations for an electron impact perpendicular to the detector entrance window at different energies. The simulations are performed with an entrance window thickness of 0.7 mm of aluminum, the value given by the manufacturer.

### 5.3. Results with $\gamma$ -ray sources

In the following paragraphs, we will present and discuss the results obtained by the measurements with the different radioactive sources. The Total-to-Peak ratio has been determined with ten different sources, whereas we used 14 different radioactive sources for the relative full-energy efficiency. These 14 sources are presented in Tab. 2. As standard calibration sources do not cover the full range of energy of interest in the present work, we produced also short-lived sources to cover the full energy range. None of the sources, except  $^{60}\text{Co}$ , had activities which were known to a precision at the per mil level. This is of course particularly true for the short-lived sources produced online. Therefore, only two  $^{60}\text{Co}$  sources with an activity known to 0.09% were used for an absolute calibration of the efficiency curve. A second method to determine the absolute efficiency, again for the  $^{60}\text{Co}$   $\gamma$  rays, used the coincident summing of the two  $\gamma$  rays.

For all standard sources, the activity is deposited on a thin plastic foil and covered with another thin foil which does not reduce in any significant way the  $\gamma$ -ray counting rate. These foils are held by a plastic frame with a diameter of 25 mm or 37 mm and thicknesses of typically 1-2 mm.

Most of the short-lived sources were produced at ISOLDE by depositing the activity, after online mass separation, on a plastic catcher of 25 mm diameter and a thickness of 4 mm. With a total energy of 40 keV, the isotopes are implanted at the surface and thus again the  $\gamma$ -ray absorption is negligible. Sources of  $^{24}\text{Na}$ ,  $^{27}\text{Mg}$ ,  $^{41}\text{Ar}$ ,  $^{48}\text{Cr}$ ,  $^{56}\text{Co}$ ,  $^{58}\text{Co}$ ,  $^{65}\text{Zn}$ ,  $^{66}\text{Ga}$ ,  $^{75}\text{Se}$ , and  $^{180}\text{Hf}^m$  were thus produced.

In addition, stronger sources of  $^{56}\text{Co}$  and  $^{66}\text{Ga}$  were produced by (p,n) reactions at the Tandem of IPN Orsay. In this case, the activity was produced over the whole target thickness (5  $\mu\text{m}$  of zinc for the  $^{66}\text{Ga}$  activity, 56  $\mu\text{m}$  of  $^{56}\text{Fe}$

for the  $^{56}\text{Co}$  source). However, dealing only with rather high  $\gamma$ -ray energies for these two sources, there was also no sensible attenuation of the  $\gamma$  rays.

#### 5.3.1. Total-to-peak ratio

To measure the Total-to-Peak (T/P) ratio, the ideal source has one  $\gamma$  ray with 100% branching ratio and no other radiation. However, such a source does not exist. From the sources used,  $^{54}\text{Mn}$  comes closest to this ideal source. The sources chosen for the T/P ratio measurement come relatively close to this ideal case, some of them emitting additional X rays, low-energy  $\beta$  particles, or 511 keV annihilation radiation. The  $^{60}\text{Co}$  source has two relatively close lying  $\gamma$  rays which can be treated as one single energy.

The sources used are the following:  $^{57}\text{Co}$ ,  $^{51}\text{Cr}$ ,  $^{85}\text{Sr}$ ,  $^{137}\text{Cs}$ ,  $^{58}\text{Co}$ ,  $^{54}\text{Mn}$ ,  $^{65}\text{Zn}$ ,  $^{60}\text{Co}$ ,  $^{22}\text{Na}$ , and  $^{41}\text{Ar}$ . Source measurements were combined with background measurements for each source.

Fig. 10 shows the experimental results. These measurements are compared first with simulations where only the germanium detector was modeled, but where the "environment" was not taken into account. Evidently, the simulated T/P ratio is significantly lower than the experimental one. Only when surrounding materials such as the measurement table, the source holder, the walls etc. are taken into account, an overall very good agreement could be obtained. The difficulty is to include this external material in CYLTRAN simulations. We achieved the good agreement shown in the figure by adding a hollow aluminum cylinder of thickness 1.6 mm and inner diameter 6.7 cm and an aluminum disk of 4 cm thickness and of radius 4.5 cm behind the source. As the detailed geometry of the backscattering material is not of interest (except if we would like to improve on the agreement between experiment and simulation of Figs. 5), we kept this backscattering configuration.

#### 5.3.2. Absolute efficiency with $^{60}\text{Co}$

The absolute efficiency for the two  $\gamma$ -ray energies of  $^{60}\text{Co}$ , i.e. 1173 keV and 1332 keV, was determined in two independent ways and with different sources. The first determination was done with two  $^{60}\text{Co}$  sources calibrated in activity with a precision of 0.09%. The second determination was done using the sum-energy peak from the coincident summing of the two  $^{60}\text{Co}$   $\gamma$  lines.

##### 5.3.2.1. Absolute efficiency with activity calibrated $^{60}\text{Co}$ sources

The procedure used in this paragraph is the standard procedure to determine the absolute efficiency of  $\gamma$ -ray detectors: knowing the activity of the source ( $A$ ), the measurement time ( $t$ ), and the branching ratios ( $BR$ ) of the  $\gamma$  rays emitted, and by determining the number of counts ( $N$ ) in the full-energy peak, the efficiency  $\epsilon^{FE}$  is determined as follows:

$$\epsilon^{FE} = \frac{N}{A \times t \times BR}.$$

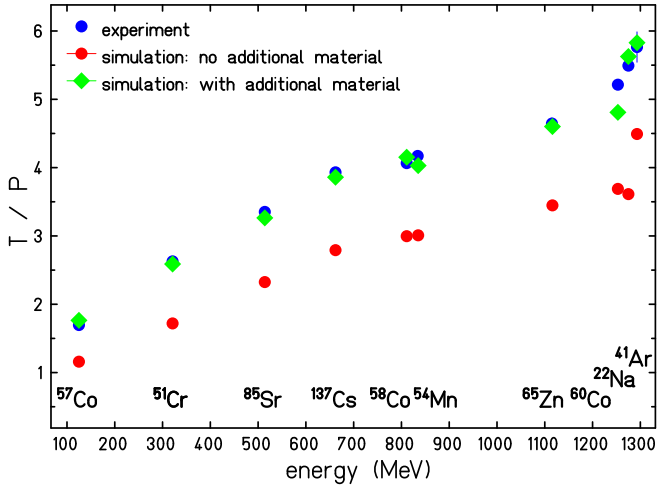


Fig. 10. Total-to-Peak ratio for  $\gamma$ -ray energies ranging from 122 keV to 1300 keV. As the measurements as well as the simulations are performed with complete decay schemes, the T/P ratio does not grow smoothly with energy. The details depend rather on the presence of other radiation. What is important is the overall good agreement between experiment and simulation.

The number of counts in the full-energy peak has to be corrected for the acquisition dead-time and pile-up effects as described above. In principle, the coincident summing effect has to be taken into account as well. However, as we only compare source data to simulations with the full decay scheme of a source, these summing effects are present in both data, the experimental data and the simulations.

The main problem in this procedure is to have a source with an activity precision of the order of 0.1%. We possess two different sources with this precision prepared by the LNHB laboratory at Saclay, France [21]. They have an absolute uncertainty on their activity of 0.09%. These sources allow us to determine the efficiency of our detector at the  $^{60}\text{Co}$   $\gamma$ -ray energies of 1173 keV and 1332 keV. These efficiencies are 0.2175(3)% at 1173 keV and 0.1996(3)% at 1332 keV.

These measurements have been performed at different periods over more than one year. During this time, the detector was warmed up at several occasions, also for longer periods of several weeks. However, we did not observe any change in efficiency and conclude thus that the efficiency is constant over time.

**5.3.2.2. Absolute efficiency from  $\gamma - \gamma$  coincidences** The absolute efficiency of a germanium detector can also be determined from  $\gamma - \gamma$  coincidences. For this purpose, one needs a source with a high-branching-ratio  $\gamma - \gamma$  cascade without any cross-over  $\gamma$  ray. The  $^{60}\text{Co}$  as well as the  $^{24}\text{Na}$  sources have these characteristics. However, the short half-life of  $^{24}\text{Na}$  prevents from using this source for this purpose.

We have performed a series of measurements with a 25 kBq  $^{60}\text{Co}$  source. By determining the number of counts in the two  $\gamma$ -ray peaks at 1173 keV and at 1332 keV as well

as in the sum peak at 2505 keV, one can establish three equations for three unknowns:

$$N_{1173} = \epsilon_{1173}^{FE} * A * BR_{1173} * (1 - \epsilon_{1332}^t * w_{12})$$

$$N_{1332} = \epsilon_{1332}^{FE} * A * BR_{1332} * (1 - \epsilon_{1173}^t * w_{12})$$

$$N_{2505} = \epsilon_{1173}^{FE} * \epsilon_{1332}^{FE} * A * BR_{2505} * w_{12}$$

$N_x$  are the numbers of counts in the full-energy peaks at energy  $x$ ,  $A$  is the source activity,  $BR_x$  is the branching ratio for the different energies ( $BR_{2505}$  is the probability to have both  $\gamma$  rays, the 1173 keV and the 1332 keV  $\gamma$  rays, in coincidence),  $\epsilon^t$  is the total efficiency, and  $w_{12}$  is the correction due to the  $\gamma - \gamma$  angular correlation.

In these equations, the three unknowns are the efficiencies at the two energies and the activity. All the other quantities are either determined from the spectrum ( $N_x$ ), from other measurements ( $\epsilon^t$ ), or from calculations ( $w_{12}$ ). In the present procedure, the acquisition dead-time as well as, to a large extent, pile-up can be neglected as they affect all peaks in the same way. However, there is one effect which has to be corrected for for the sum peak. This is the probability that a 1173 keV  $\gamma$  ray from one event is added to a 1332 keV  $\gamma$  ray from another event and vice versa and add to the sum energy peak at 2505 keV. This effect is not negligible, as can be seen from the presence of small but visible peaks at 2346 keV and 2664 keV, twice the energies of the individual  $\gamma$  rays. We used the counting rates in these two sum peaks, corrected for the detection efficiency of the respective other  $\gamma$ -ray energy, and determined thus the number of counts to be subtracted from the 2505 keV sum peak.

The angular correlation correction  $w_{12}$  was determined in a Monte-Carlo simulation with the CYLTRAN code, where we compared the sum energy peak in a simulation with angular correlation to a simulation for an isotropic emission of the  $\gamma$  rays. The result of these simulations is quite close to a calculation of the angular correlation correction at a fixed angle of  $0^\circ$  which does not take into account the opening angle of the detector and thus the contribution of  $\gamma - \gamma$  angles larger than zero.

From our data, we determine efficiencies of 0.2186(7)% and 0.1996(7)% at 1173 keV and 1332 keV, respectively. These efficiencies are in excellent agreement with the values determined with the high-precision sources. The precision is somewhat less than from the high-precision sources. This is exclusively due to the fact that one needs a high number of counts in the sum energy peak and this implies very long measuring times. In our case, we performed measurements over several months.

**5.3.2.3. Final efficiency for the  $^{60}\text{Co}$   $\gamma$ -ray energies** From both the above methods to determine the absolute efficiency for the  $^{60}\text{Co}$   $\gamma$  rays, we arrive at a final efficiency of 0.2177(4)% and 0.1996(3)% at 1173 keV and 1332 keV, respectively. These experimental efficiencies can be compared to the results of our MC simulations of 0.2174(3)% and 0.1997(3)%. This precision corresponds to about 1.5-2 ‰.

### 5.3.3. Full-energy peak efficiency with other sources

The sources used for the determination of the full-energy efficiency curve are given in Tab. 2 with the information pertinent for the present work. These sources cover an energy range from 30 keV to 3.4 MeV. In our work we did not use the 500 keV  $\gamma$  ray of  $^{180}\text{Hf}^m$  and the two highest energy  $\gamma$ -ray lines of  $^{66}\text{Ga}$ . These  $\gamma$  rays were already rejected in the work of Hardy and co-workers [2–4]. They have an apparent wrong branching ratio in the literature.

As already mentioned, all sources were used to establish the relative full-energy peak efficiency, their activity being treated as a free parameter in the fitting of the relative efficiency curve. This was necessary because none of the sources (except the two  $^{60}\text{Co}$  sources) is available with a precision on the activity necessary for the present work. However, our procedure allows us to determine with good accuracy the activity of these sources. A comparison of the activities determined and those given by the manufacturers is shown in Tab. 3.

Table 3

Comparison between the activity of commercial sources as given by the manufacturers and the activity determined in our fitting procedure. The factor given in the table is the ratio between the activity given by the manufacturer and the one determined by our means. The error bars are 1-sigma error bars.

source	$^{133}\text{Ba}$	$^{207}\text{Bi}$	$^{134}\text{Cs}$	$^{137}\text{Cs}$	$^{152}\text{Eu}$	$^{88}\text{Y}$
factor	1.034(9)	1.012(5)	1.009(40)	1.020(11)	1.014(13)	1.069(8)

Fig. 11a shows the efficiency curve as determined from the sources with a maximum of the efficiency of about 1% at 60 keV (this curve is already adjusted in absolute height with the  $^{60}\text{Co}$  sources, see above). A much more detailed picture is shown in Fig. 11b, where we present the difference between the experimental efficiency and the simulated one normalised by the experimental efficiency. Although some points lie somewhat far from the zero-difference line, the vast majority of the data points lie within the  $\pm 1\%$  boundaries. A fit with a constant of these differences between experiment and simulations yields a value of  $(-0.002 \pm 0.061)\%$  with a normalised  $\chi^2$  of 1.4. A linear fit gives a linear term of  $(0.16 \pm 0.16)$  compatible with zero. The normalised  $\chi^2$  does not change, another indication that the addition of a linear term does not improve the fit. If we remove, for a test, the data points below 50 keV, we obtain a value of  $(0.07 \pm 0.16)$  for the linear term which shows that the possible slight trend is entirely due to the low-energy points which are extremely difficult to fit in a  $\gamma$ -ray spectrum.

We investigated also, whether we get better agreement in the low- or high-energy region. Therefore, we fitted the difference data in the region below 1500 keV and above 1000 keV. For the low-energy region, we get an average value for the difference of  $(-0.010 \pm 0.077)\%$ , whereas the result for the high-energy part is  $(-0.009 \pm 0.083)\%$ . In both cases, a linear fit does not improve the results.

As the result of our MC simulations exactly fits our measured efficiencies for the  $^{60}\text{Co}$  source and the ratio between experimental results and simulations are constant with en-

ergy, we conclude that we have obtained a precision on the efficiency simulation of our detector below 0.1% over a wide energy range. To be conservative, we attribute an uncertainty of 0.5% to our efficiency below 100 keV and of 0.1% between 100 keV and 3.4 MeV for the relative efficiencies. If we combine the uncertainty of the efficiencies for the  $^{60}\text{Co}$   $\gamma$  rays with the uncertainty of these relative efficiencies, we find an uncertainty of 0.5 % below 100 keV and of 0.15 % above.

These values can be used now in experiments for the  $\gamma$ -ray efficiency precision of the detector installed at exactly 15 cm from the radioactive source. This is indeed the case, as the detector was used in two experiments at GANIL, one on LISE3 and one at the SPIRAL identification station [22], and in an experiment at the IGISOL4 facility of Jyväskylä.

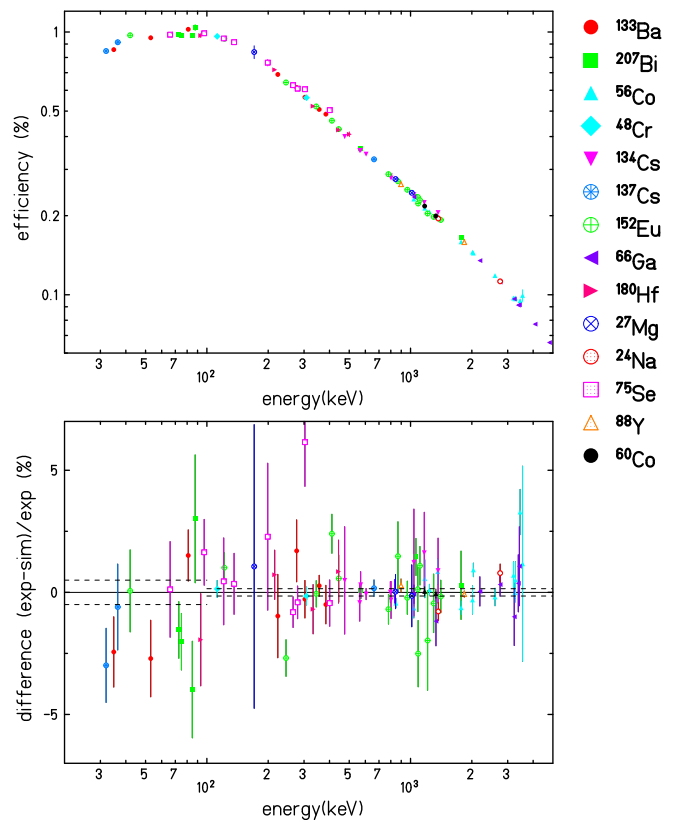


Fig. 11. (a) Absolute  $\gamma$ -ray efficiency at a distance of 15 cm between the source and the detector entrance window. As explained in the text, the shape of the curve is determined with the  $\gamma$  rays given in Tab. 2, whereas the absolute height of the curve was determined by means of  $^{60}\text{Co}$  sources. The curve is not completely smooth, as what is presented is not the single  $\gamma$ -ray efficiencies, but full-energy peak efficiencies determined with the complete decay schemes from the sources. (b) Relative differences (in %) between the experimental data and the simulations with the detector model are presented. The dashed lines give the final precisions adopted.

## 6. Conclusions

In the present work, we have combined source measurements and simulations to develop a germanium detector

model which allows to describe the experimental results with simulations. For this purpose, a total of 23 different radioactive sources have been used. The detector model was established with scans of the germanium crystal and then compared to the source measurements.

This work demonstrates that we have been able to efficiently calibrate our single-crystal high-purity germanium detector with a precision of 0.15 % between 100 keV and 3.4 MeV and of 0.5 % below 100 keV. This allows us now to determine branching ratios of e.g. super-allowed  $\beta$  decay with a similar precision.

The detector model was mainly developed with the aid of the CYLTRAN program package. However, the detector model was transposed recently to the GEANT4 program package and yields results in perfect agreement with the CYLTRAN simulations. The GEANT4 software has the advantage that more complicated experimental situations can be modelled more correctly. However, for the moment, the CYLTRAN description was found to be sufficiently precise for our applications. In addition, the CYLTRAN simulations are much faster than the GEANT4 simulations.

As the detector was already used and will be used in the future in different experimental environments, each new experimental arrangement requires a new measurement of the total-to-peak ratio. Therefore, relatively simple sources have to be used under online conditions to achieve this. Typically, sources of  $^{57}\text{Co}$ ,  $^{54}\text{Mn}$ , and  $^{60}\text{Co}$  are used for this purpose.

## Acknowledgment

We are grateful to A. Korichi and H. Ha for their help with the detector scan at CSNSM. We thank K. Johnston, A. Gottberg, and G. Correia from ISOLDE for their help during the sample collection at ISOLDE. Our gratitude goes also to the accelerator staff at IPN Orsay. We are in debt to J.L. Tain for providing us with his  $\gamma$ - $\gamma$  correlation program and the basic version of the event generator program. We are grateful to C. Serna for his help with the electron source.

## References

- [1] J. C. Hardy and I. S. Towner, *Phys. Rev. C* **79**, 055502 (2009).
- [2] J. C. Hardy *et al.*, *Int. J. Appl. Rad. Isot.* **56**, 65 (2002).
- [3] R. G. Helmer *et al.*, *Nucl. Instrum. Meth. A* **511**, 360 (2003).
- [4] R. G. Helmer, N. Nica, J. C. Hardy, and V. E. Jacob, *Int. J. Appl. Rad. Isot.* **60**, 173 (2004).
- [5] J. A. Halbleib and T. A. Mehlhorn, *Nucl. Sci. Eng.* **92**, 338 (1986).
- [6] S. Agostinelli *et al.*, *Nucl. Instrum. Meth. A* **506**, 250 (2003).
- [7] <http://wiki.ganil.fr/gap/>.
- [8] <http://caeinfo.in2p3.fr/article273.html>.
- [9] G. F. Grinyer *et al.*, *Nucl. Instrum. Meth. A* **579**, 1005 (2007).
- [10] R. Firestone, *Table of Isotopes*, **8th Edition**, 1996.
- [11] <http://root.cern.ch/drupal/content/download>.
- [12] <http://www.nndc.bnl.gov/ensdf/>.
- [13] G. Audi *et al.*, *Chin. Phys. C* **36**, 1287 (2012).
- [14] IAEA STI/PUB/1287-VOL1 (2007).
- [15] IAEA-TECDOC-619 (1991).
- [16] M. Shibata *et al.*, *Int. J. Appl. Radiat. Isot.* **49**, 985 (1998).
- [17] G. W. Severin, L. D. Knutson, P. A. Voytas, and E. A. George, *Phys. Rev. C* **82**, 067301 (2010).
- [18] C. M. Baglin *et al.*, *Nucl. Instrum. Meth. A* **481**, 365 (2002).
- [19] T. Ha *et al.*, *Nucl. Instrum. Meth. A* **697**, 123 (2013).
- [20] CN/ASD Group, PAW Users Guide, CERN Program Library Q121, CERN 1993.
- [21] <http://www-centre-saclay.cea.fr/fr/Laboratoire-national-Henri-Becquerel-LNHB>.
- [22] G. F. Grinyer *et al.*, *Nucl. Instrum. Meth. A* **741**, 18 (2014).